Technical Note

1975-20

R. L. Bagley

Applications of the Principle of Dynamic Equipollency to Mechanical Admittance Testing

10 March 1975

Lincoln Laboratory

MASSACHUSETTS INSTITUTE OF TECHNOLOGY
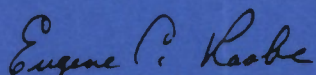
LEXINGTON, MASSACHUSETTS

This technical report has been reviewed and is approved for publication.

FOR THE COMMANDER

Eugene C. Raabe, Lt. Col., USAF
Chief, ESD Lincoln Laboratory Project Office

MASSACHUSETTS INSTITUTE OF TECHNOLOGY

LINCOLN LABORATORY

APPLICATIONS OF THE
PRINCIPLE OF DYNAMIC EQUIPOLLENCY TO
MECHANICAL ADMITTANCE TESTING

R. L. BAGLEY

Group 73

LEXINGTON   MASSACHUSETTS

ABSTRACT

The principle of dynamic equipollency is defined
and applied to two areas of mechanical admittance/
impedance testing: generation of experimental
moment-rotational velocity admittances and im-
pedances, and many-DOF structures.

TABLE OF CONTENTS

LIST OF FIGURES

LIST OF TABLES

LIST OF SYMBOLS

$\{a\}$	column matrix of modal participation coefficients
c	a constant
$D_\ell(\omega)$	ℓ th modal damping function
E	Young's Modulus
$\{f\}$	column matrix of applied forces
$\left\{\dfrac{f_1}{f_2}\right\}$	applied forces at each DOF subset
i	imaginary coefficient
I	second moment of area of the cross section of the beam
$[K]$	stiffness matrix
$[K_{11}]$	stiffness matrix for the first DOF subset
$[K_{11}]_n$	stiffness matrix for the first DOF subset for the nth substructure
$[K_{33}]$	stiffness matrix for the DOF encompassed by the reduced mode shapes of the structure
$[K]_T$	stiffness matrix for the total structure
R	length of lever arm (Fig. 9)
L	total number of DOF for a structure or substructure
m_ℓ	ℓ th modal mass
$[M]$	mass matrix
$[M_{11}]$	mass matrix for the first DOF subset
$[M_{11}]_n$	mass matrix for the first DOF subset for nth substructure

$[M_{33}]$	mass matrix for the DOF encompassed by the reduced mode shapes of the structure
$[M]_T$	mass matrix for the total structure
$\{v\}$	column matrix of resultant velocities of the structure's DOF
$\left\{\dfrac{v_1}{v_2}\right\}$	column matrix of resultant velocities partitioned to show the velocities of each DOF subset
$\{x_3\}$	displacements at the DOF on the interfaces of a substructure
Y_{jK}	jK^{th} admittance
$[Y]$	admittance matrix
$\begin{bmatrix} Y_{11} & Y_{12} \\ \hline Y_{21} & Y_{22} \end{bmatrix}$	admittance matrix partitioned corresponding to DOF subsets
Z_{jK}	jK^{th} impedance
$[Z]$	impedance matrix
$[Z_{33}]_n$	impedance matrix for the DOF encompassed by the reduced mode shapes of the nth substructure
$[Z]_T$	impedance matrix of the total structure
β_n	parameter of a beam based on its length and displacement boundary conditions
$\Theta, \dot{\Theta}$	rotation in radians, and its first time derivation, respectively
λ	number of resonant frequencies or mode shapes of a structure

μ_ℓ square root of the ℓth modal mass

ν_n n^{th} resonant frequency expressed in cps

ρ mass per unit length of a beam

ϕ_j^ℓ j^{th} component of the ℓth mode shape

$\{\phi_n^\ell\}$ ℓ^{th} mode shape for the nth DOF subset

$\left\{\dfrac{\phi_n^\ell}{\mu_\ell}\right\}$ normalized ℓ^{th} mode shape for the nth DOF subset

$[\phi_n]$ modal matrix for the nth DOF subset

$\left[\dfrac{\phi_n}{\mu}\right]$ normalized modal matrix for the nth DOF subset

$\left\{\dfrac{\phi_3^\ell}{\mu_\ell}\right\}$ ℓ^{th} reduced mode shape

$\left[\dfrac{\phi_3}{\mu}\right]$ modal matrix of reduced modes

$\left\{\dfrac{\phi^\ell}{\mu_\ell}\right\}_n$ ℓ^{th} normalized mode shape of the nth substructure

$[\dfrac{\phi}{\mu}]_n$ normalized modal matrix for the nth substructure

$\left\{\dfrac{\phi^\ell}{\mu_\ell}\right\}_T$ ℓ^{th} normalized mode shape of the total structure

$\left|\dfrac{'\phi^\ell}{\mu_\ell}\right|_{T_3}$ $\left|\dfrac{\phi^\ell}{\mu_\ell}\right|_{T_I}$ column matrix of the total structure's ℓ^{th} normalized mode shape at the interfaces and interior, respectively, of a substructure

ω frequency of excitation in radians per second

ω_ℓ ℓ^{th} resonant frequency in radians per second

$[\ ]$ square or rectangular matrix

$[\ ]^{-1}$ inverse matrix

$[\ ]^{T}$ transpose matrix

$\lfloor\ \rfloor$ row matrix

$\{\ \}$ column matrix

$|\ |$ absolute value or magnitude

APPLICATIONS OF THE PRINCIPLE OF DYNAMIC EQUIPOLLENCY TO MECHANICAL ADMITTANCE TESTING

INTRODUCTION

The principle of dynamic equipollency (DE) is the relationship between two sets of forces applied at two separate subsets of a structure's degrees of freedom (DOF). This report illustrates and elucidates applications of the DE principle, as proposed in Lincoln Laboratory Technical Note 1974-17,[1] to two weak areas of mechanical admittance/impedance techniques: (a) many DOF structures, and (b) experimental generation of moment-rotational velocity impedances.

The DE principle is applied to a structure with 25 DOF to determine the structure's first two mode shapes and resonant frequencies, greatly reducing the number of measured mechanical admittances required to characterize a many-DOF structure.

Also, moment-rotational velocity impedances, determined from measured admittances via the DE principle, make possible the assembly of substructures into a total structure ensuring the compatibility of rotational as well as lateral displacements at interfaces. Two beam structures are assembled mathematically using experimentally determined impedances.

It is important that the reader have a basic understanding of mechanical admittance/impedance concepts.[2] It is also desirable for the reader to be familiar with the inverse eigenvalue method of mechanical admittance analysis, a method of solving for a structure's mass and stiffness matrices from mechanical admittance measurements.[3]

CHAPTER I
PRINCIPLE OF DYNAMIC EQUIPOLLENCY

When the number of mode shapes of a large complex structure is less than the number of locations on the structure (characterized as DOF) where dynamic behavior is important, certain problems are encountered with the structure's admittance matrix. The order of the admittance matrix is equal to the number of DOF where admittance measurements are made and the rank of the admittance matrix is equal to the number of mode shapes (rigid body and elastic). In this case, the order of the admittance matrix is greater than the rank of the admittance matrix. Consequently, the admittance matrix is singular and its inverse, the impedance matrix, does not exist.

The columns (rows) of this singular admittance matrix are linear combinations of fewer mode shapes than there are columns (rows) in the matrix. It follows that there must exist relationships among the columns (rows) of the admittance matrix.[4] These relationships are determined using a linear, modal model of the structure.

Equation (1) is an expression of the velocities at all of the structure's DOF, $\{v\}$, resulting from the applied forces given in the column matrix $\{f\}$. L, the number of DOF, is greater than λ, the number of mode shapes of the structure:

$$\{v\} = \sum_{\ell=1}^{\lambda} \frac{\frac{\omega}{m_\ell} \lfloor \phi^\ell \rfloor \{f\}}{i(\omega^2 - \omega_\ell^2) + D_\ell(\omega)} \{\phi^\ell\} \tag{1}$$

where

$\{\phi^\ell\} = \ell^{th}$ mode shape of the structure, $\ell = 1, 2, 3 \ldots \lambda$

$m_\ell = \ell^{th}$ modal mass

$\omega_\ell = \ell^{th}$ resonant frequency expressed in radians per second

$D_\ell(\omega) = \ell^{th}$ modal damping function.

2

The column matrices $\{\phi^\ell\}$, $\{f\}$ and $\{v\}$ have L elements. Each column matrix is partitioned into two subcolumn matrices corresponding to two mutually exclusive, collectively exhaustive subsets of the structure's DOF. The first subset is the DOF $\ell = 1, 2, 3 \ldots \lambda$, and the second subset is the DOF $\ell = \lambda + 1, \lambda + 2, \lambda + 3, \ldots L$.

$$\{\phi^\ell\} = \left\{ \frac{\phi^\ell_1}{\phi^\ell_2} \right\} \tag{2}$$

$$\{v\} = \left| \frac{v_1}{v_2} \right| \tag{3}$$

$$\{f\} = \left| \frac{f_1}{f_2} \right| \quad . \tag{4}$$

Equation (5) is Eq. (1) expressed using Eqs. (2), (3) and (4):

$$\left| \frac{v_1}{v_2} \right| = \sum_{\ell=1}^{\lambda} \frac{\frac{\omega}{m_\ell} \lfloor \phi^\ell_1 \vdots \phi^\ell_2 \rfloor \left| \frac{f_1}{f_2} \right|}{i(\omega^2 - \omega_\ell^2) + D_\ell(\omega)} \left\{ \frac{\phi^\ell_1}{\phi^\ell_2} \right\} \tag{5}$$

$$\left| \frac{v_1}{v_2} \right|_1 = \sum_{\ell=1}^{\lambda} \frac{\frac{\omega}{m_\ell} \lfloor \phi^\ell_1 \vdots \phi^\ell_2 \rfloor \left| \frac{f_1}{0} \right|}{i(\omega^2 - \omega_\ell^2) + D_\ell(\omega)} \left\{ \frac{\phi^\ell_1}{\phi^\ell_2} \right\} \tag{6}$$

$$\left| \frac{v_1}{v_2} \right|_2 = \sum_{\ell=1}^{\lambda} \frac{\frac{\omega}{m_\ell} \lfloor \phi^\ell_1 \vdots \phi^\ell_2 \rfloor \left| \frac{0}{f_2} \right|}{i(\omega^2 - \omega_\ell^2) + D_\ell(\omega)} \left\{ \frac{\phi^\ell_1}{\phi^\ell_2} \right\} \quad . \tag{7}$$

Equations (6) and (7) represent cases where forces are applied only at the first DOF subset, and only at the second DOF subset, respectively. If the relationship in Eq. (8) is satisfied, the dynamic response of the structure is the same for the two cases shown in Eqs. (6) and (7):

$$\lfloor \phi^\ell_1 \vdots \phi^\ell_2 \rfloor \left| \frac{f_1}{0} \right| = \lfloor \phi^\ell_1 \vdots \phi^\ell_2 \rfloor \left| \frac{0}{f_2} \right| \qquad \ell = 1, 2, 3 \ldots \lambda \quad . \tag{8}$$

3

Equation (9) is Eq. (8) simplified:

$$\lfloor \phi_1^\ell \rfloor \{f_1\} = \lfloor \phi_2^\ell \rfloor \{f_2\} \qquad \ell = 1, 2, 3 \ldots \lambda \quad . \tag{9}$$

The set of λ equations shown in Eq. (9) are consolidated into one matrix equation in Eq. (10).

$$[\phi_1]^T \{f_1\} = [\phi_2]^T \{f_2\} \quad . \tag{10}$$

The matrix $[\phi_2]^T$ is, in general, rectangular and has rows that are the structure's mode shapes at the second DOF subset. $[\phi_1]^T$ is a square matrix and its rows are the structure's mode shapes at the first DOF subset. Since $[\phi_1]^T$ is square and its rows are λ, linearly independent mode shapes, then $[\phi_1]^{T-1}$ exists:

$$\{f_1\} = [\phi_1]^{T-1} [\phi_2]^T \{f_2\} \quad . \tag{11}$$

Equation (11) states that given any set of forces applied at the second DOF subset, $\{f_2\}$, one can solve for a set of forces to be applied at the first DOF subset, $\{f_1\}$, that produces the same dynamic response of the structure. This is the DE principle.

The structure's admittance matrix is partitioned in Eq. (12) according to the previously mentioned DOF subsets:

$$\left\{ \frac{v_1}{v_2} \right\} = \left[\begin{array}{c|c} Y_{11} & Y_{12} \\ \hline Y_{21} & Y_{22} \end{array} \right] \left\{ \frac{f_1}{f_2} \right\} \tag{12}$$

$$\left\{ \frac{v_1}{v_2} \right\}_1 = \left[\begin{array}{c|c} Y_{11} & Y_{12} \\ \hline Y_{21} & Y_{22} \end{array} \right] \left\{ \frac{f_1}{0} \right\} \tag{13}$$

$$\left\{ \frac{v_1}{v_2} \right\}_2 = \left[\begin{array}{c|c} Y_{11} & Y_{12} \\ \hline Y_{21} & Y_{22} \end{array} \right] \left\{ \frac{0}{f_2} \right\} \quad . \tag{14}$$

It has already been shown that the two sets of applied forces $\{f_1\}$ and $\{f_2\}$ can be determined such that they produce the same dynamic response of the structure. Equations (13) and (14) can now be used to determine relationships among

the columns (rows) of the structure's admittance matrix. The columns (rows) are expressed collectively as submatrices:

$$\left[\begin{array}{c|c} Y_{11} & Y_{12} \\ \hline Y_{21} & Y_{22} \end{array}\right] \left\{\frac{f_1}{0}\right\} = \left\{\frac{v_1}{v_2}\right\}_1 = \left\{\frac{v_1}{v_2}\right\}_2 = \left[\begin{array}{c|c} Y_{11} & Y_{12} \\ \hline Y_{21} & Y_{22} \end{array}\right] \left\{\frac{0}{f_2}\right\} \tag{15}$$

$$\left[\frac{Y_{11}}{Y_{21}}\right] \{f_1\} = \left[\frac{Y_{12}}{Y_{22}}\right] \{f_2\} \tag{16}$$

$$[Y_{11}] \{f_1\} = [Y_{12}] \{f_2\} \tag{17}$$

$$[Y_{21}] \{f_1\} = [Y_{22}] \{f_2\} \quad . \tag{18}$$

Equation (19), derived from Eq. (17), is similar to Eq. (11):

$$\{f_1\} = [Y_{11}]^{-1} [Y_{12}] \{f_2\} \tag{19}$$

$$\{f_1\} = [\phi_1]^{T-1} [\phi_2]^{T} \{f_2\} \tag{11}$$

$$[Y_{12}] = [Y_{21}]^{T} \quad . \tag{20}$$

Equations (11) and (19) and the symmetry of the admittance matrix, Eq. (20), relate measured admittances to the structure's mode shapes, Eq. (21):

$$[\phi_1]^{T-1} [\phi_2]^{T} = [Y_{11}]^{-1} [Y_{21}]^{T} \quad . \tag{21}$$

The matrix $[Y_{11}]^{-1}$ can be calculated from $[Y_{11}]$ except when $[Y_{11}]$ is measured at a resonant frequency of the structure.

Equation (21) shows that the matrix product $[Y_{11}]^{-1} [Y_{21}]^{T}$ is invariant with respect to the frequency of excitation. It is important to remember that one of the assumptions leading to Eq. (21) is that the structure has only a finite number, λ, of mode shapes. In general, the elements of $[Y_{11}]$ and $[Y_{21}]$ are functions of the frequency of excitation. Equation (21) yields Eq. (22) and is used in Chap. II to solve for the mode shapes of a 25-DOF beam structure:

$$[\phi_2]^{T} = [\phi_1]^{T} [Y_{11}]^{-1} [Y_{21}]^{T} \quad . \tag{22}$$

5

The DE principle can be used to determine the relationship among all the submatrices of the structure's admittance matrix. Substituting Eq. (19) into Eq. (18) gives Eq. (23):

$$[Y_{21}] [Y_{11}]^{-1} [Y_{12}] \{f_2\} = [Y_{22}] \{f_2\} \quad . \tag{23}$$

Equation (23) yields Eq. (24) which is the relationship among the submatrices of the admittance matrix:

$$[Y_{21}] [Y_{11}]^{-1} [Y_{12}] = [Y_{22}] \quad . \tag{24}$$

Equation (25) is derived using the symmetry of the structure's admittance matrix, Eq. (20), and the relationship in Eq. (24):

$$[Y_{21}] \cdot [Y_{11}]^{-1} \cdot [Y_{21}]^T = [Y_{22}] \quad . \tag{25}$$
$$(L-\lambda) \times \lambda \quad \lambda \times \lambda \quad \lambda \times (L-\lambda) \quad (L-\lambda) \times (L-\lambda)$$

The number of elements in each matrix is given under each matrix.

As before, λ is the number of modes of the structure and L is the number of DOF for the structure where $L > \lambda$. If L is much greater than λ, it can be seen from Eq. (25) that it is much more efficient to measure the elements of $[Y_{11}]$ and $[Y_{21}]$ ($\lambda \times L$ total elements) and calculate $[Y_{22}]$ using Eq. (25) rather than measure the $(L-\lambda)^2$ total elements of $[Y_{22}]$.

Equation (25) can also be used to calculate moment-rotational velocity admittances. If the second DOF subset is rotational DOF and $[Y_{21}]$ is measured using rotational sensors at the second DOF subset, $[Y_{22}]$ calculated using Eq. (25) is comprised of moment-rotational velocity admittances:

$$[Y_{21}] \cdot [Y_{11}]^{-1} \cdot [Y_{21}]^T = [Y_{22}] \tag{25}$$

$$(\text{lb-sec})^{-1} \cdot (\frac{\text{lb-sec}}{\text{in.}}) \cdot (\text{lb-sec})^{-1} = (\text{lb-in.-sec})^{-1} \quad . \tag{26}$$

The physical dimensions of each matrix in Eq. (25) are given directly under it in Eq. (26). Equation (26) shows that $[Y_{22}]$ has the physical dimensions of moment-rotational velocity admittances. The experimental determination and application of moment-rotational velocity admittances are the subjects of Chaps. III and IV.

6

CHAPTER II
DETERMINATION OF MODE SHAPES FOR A 25-DOF STRUCTURE

A 6-ft, clamped-clamped beam structure is characterized as having
25 DOF, L = 25 (Fig. 1). The aluminum channel beam is clamped at both ends
to a steel support. The structure is assumed to have two mode shapes, λ = 2,
that dominate the structure's low frequency (less than 150 Hz) dynamic behavior.
The first DOF subset is DOFs 10 and 16. The second DOF subset consists of
all the remaining DOFs.
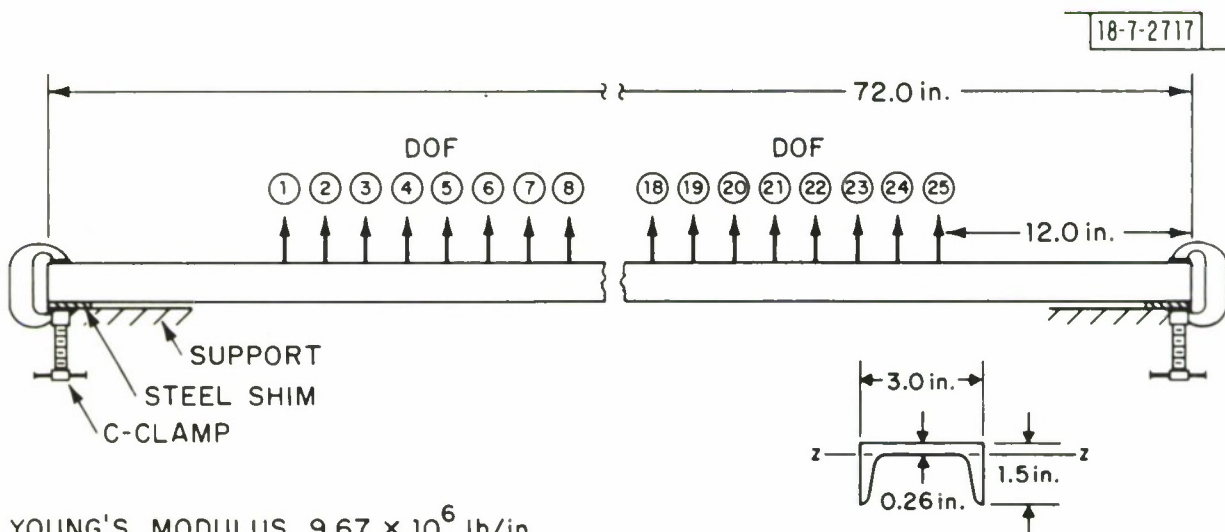
YOUNG'S MODULUS 9.67×10^6 lb/in.
MOMENT OF AREA, I_{zz} 0.25 in.^{4}
MASS PER UNIT LENGTH 3.74×10^{-4} slug/in.
LENGTH 72.0 in.

Fig. 1. Six-ft, clamped-clamped, 25-DOF beam structure.
All DOF are 2-in. apart.

The DOFs on the structure are chosen such that no axial or tortional motion
of the beam is generated while the admittances are measured. The Wilcoxon
Research F3 shaker and Z602 impedance head assembly generate and measure
the applied force and resultant motion of the structure.[5] The admittances are
generated by a Spectral Dynamics Corporation SD-1002B-33 automatic me-
chanical impedance system (Fig. 2).[6] A piezoelectric accelerometer measures
motion of the structure at DOFs other than the one where the force is applied.
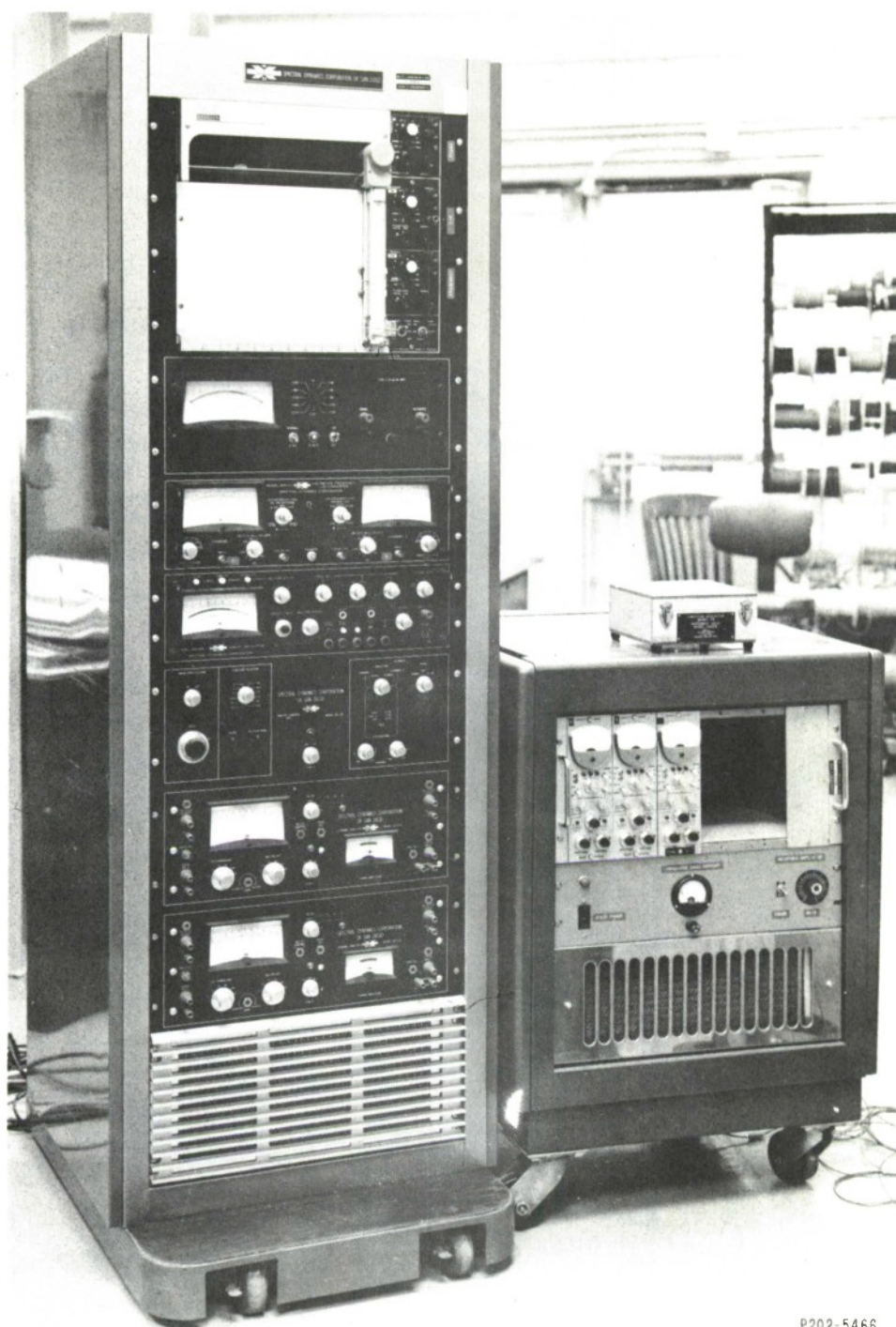
Fig. 2. SD1002B-33 automatic mechanical impedance system (left) and power and charge amplifiers (right).

P202-5466

8

The shaker/impedance head is placed at DOF 16 and the mutual admittance and all cross admittances are measured. Since DOFs 10 and 16 are equidistant from the center of the beam and the beam is symmetric about its center, the motion of the beam with the shaker/impedance head attached at DOF 10 is a mirror image of the motion of the structure with the shaker/impedance head attached at DOF 16. The admittances measured with the shaker/impedance head at DOF 16 are converted to admittances of the structure with the shaker/impedance head attached at DOF 10 using the scheme shown in Eq. (27):

$$Y_{S\,16} = Y_{26-S\,10} \quad . \tag{27}$$

Values chosen from the mutual and cross admittances measured for the first DOF subset, DOFs 10 and 16, are used to calculate mass and stiffness matrices of the structure. The mass and stiffness matrices are calculated using the inverse eigenvalue method:[7]

$$[M] = \begin{bmatrix} 8.75 & -3.29 \\ -3.29 & 8.75 \end{bmatrix} 10^{-3} \text{ slug} \tag{28}$$

$$[K] = \begin{bmatrix} 4.89 & -4.28 \\ -4.28 & 4.89 \end{bmatrix} 10^{3} \text{ lb/in.} \quad . \tag{29}$$

The mode shapes for DOFs 10 and 16 and the resonant frequencies of the structure are calculated from the mass and stiffness matrices using the iterative method.[8] The resonant frequencies calculated from the experimentally determined mass and stiffness matrices are in good agreement with the resonant peaks observed in the measured admittances. This lends credence to the accuracy of the experimentally determined mass and stiffness matrices:

$$\{\phi_1^1\} = \begin{Bmatrix} 1.0 \\ 1.0 \end{Bmatrix} \quad ; \quad \nu_1 = \frac{\omega_1}{2\pi} = 53.2 \text{ Hz} \tag{30}$$

$$\{\phi_1^2\} = \begin{Bmatrix} 1.0 \\ -1.0 \end{Bmatrix} \quad ; \quad \nu_2 = \frac{\omega_2}{2\pi} = 139 \text{ Hz} \quad . \tag{31}$$

9

Equation (22) is used to calculate the components of the structure's mode shapes at the second DOF subset.

$$[\phi_2]^T = [\phi_1]^T [Y_{11}]^{-1} [Y_{21}]^T \quad . \tag{22}$$

$[\phi_1]^T$ is constructed from Eqs. (30) and (31). $[Y_{11}]$ and $[Y_{21}]^T$ are constructed from the admittances measured at 70 Hz. The subscripts of the measured admittances show the position of the measured admittances in matrices $[Y_{11}]$ and $[Y_{21}]^T$ in Eqs. (33) and (34):

$$[\phi_1]^T = \begin{bmatrix} 1.0 & 1.0 \\ 1.0 & -1.0 \end{bmatrix} \tag{32}$$

$$[Y_{11}] = \begin{bmatrix} 4.61 & 5.29 \\ 5.29 & 4.61 \end{bmatrix} \cdot (-10^{-1}) \, i \qquad \begin{bmatrix} 10,10 & 10,16 \\ 16,10 & 16,16 \end{bmatrix} \tag{33}$$

$$[Y_{21}]^T = \begin{bmatrix} 1.5 \ 1.8 \ 2.3 \ 2.6 \ 3.1 \ 3.5 \ 3.8 \ 4.1 \ 4.3 \ 4.7 \ 5.1 \ 5.3 \ 5.3 \ 5.3 \\ 2.2 \ 2.6 \ 3.2 \ 3.6 \ 4.1 \ 4.4 \ 4.8 \ 5.1 \ 5.3 \ 5.3 \ 5.3 \ 5.3 \ 5.1 \ 4.7 \end{bmatrix}$$

$$\begin{bmatrix} 5.3 \ 5.1 \ 4.8 \ 4.4 \ 4.1 \ 3.6 \ 3.2 \ 2.6 \ 2.2 \\ 4.3 \ 4.1 \ 3.8 \ 3.5 \ 3.1 \ 2.6 \ 2.3 \ 1.8 \ 1.5 \end{bmatrix} \cdot (-10^{-1}) \, i$$

$$\begin{bmatrix} 1,10 \ 2,10 \ 3,10 \ 4,10 \ 5,10 \ 6,10 \ 7,10 \ 8,10 \ 9,10 \ 11,10 \\ 1,16 \ 2,16 \ 3,16 \ 4,16 \ 5,16 \ 6,16 \ 7,16 \ 8,16 \ 9,16 \ 11,16 \end{bmatrix}$$

$$\begin{bmatrix} 12,10 \ 13,10 \ 14,10 \ 15,10 \ 17,10 \ 18,10 \ 19,10 \ 20,10 \\ 12,16 \ 13,16 \ 14,16 \ 15,16 \ 17,16 \ 18,16 \ 19,16 \ 20,16 \end{bmatrix}$$

$$\begin{bmatrix} 21,10 \ 22,10 \ 23,10 \ 24,10 \ 25,10 \\ 21,16 \ 22,16 \ 23,16 \ 24,16 \ 25,16 \end{bmatrix} \quad . \tag{34}$$

$[Y_{11}]^{-1}$ is calculated and then $[\phi_2]^T$ is calculated from $[\phi_1]^T$, $[Y_{21}]^T$ and $[Y_{11}]^{-1}$, Eq. (22). The calculated mode shapes for the clamped-clamped beam structure, normalized by the largest component of the mode, are compared to the modes of a clamped-clamped continuum beam (Figs. 3, 4 and Table 1). (See the Appendix for methods used to calculate the mode shapes of the clamped-clamped continuum beam.)

The values calculated for the second-mode shapes, $\{\phi^2\}$, are less accurate than those values calculated for the first-mode shape, $\{\phi^1\}$. The frequency of excitation for the values of $[Y_{11}]$ and $[Y_{21}]$ used to calculate $[\phi_2]^T$ is 70 Hz. This frequency is relatively close to the first resonant frequency of the structure, 50 Hz, and relatively far from the second resonant frequency, 138 Hz. Consequently, the participation of the first mode is much greater than participation of the second in the admittance matrices $[Y_{11}]$ and $[Y_{21}]$.

$[Y_{11}]$ and $[Y_{21}]$ are measured at a frequency of excitation, 126 Hz, relatively close to the second resonant frequency of the structure. $[Y_{11}]$ and $[Y_{21}]^T$ measured at 126 Hz are given in Eqs. (35) and (36):

$$[Y_{11}] = \begin{bmatrix} 0.93 & -3.72 \\ -3.72 & 0.93 \end{bmatrix} 10^{-1} i \tag{35}$$

$$[Y_{21}]^T = \begin{bmatrix} 1.8 & 2.5 & 2.7 & 2.8 & 2.9 & 2.7 & 2.5 & 2.3 & 1.9 & 0.6 \\ -3.5 & -4.1 & -4.9 & -5.0 & -5.5 & -6.0 & -5.4 & -4.8 & -4.6 & -3.3 \end{bmatrix}$$

$$\begin{matrix} -0.5 & -1.6 & -2.5 & -3.3 & -4.6 & -4.8 & -5.4 & -6.0 & -5.5 & -5.0 \\ -2.5 & -1.6 & -0.5 & 0.6 & 1.9 & 2.3 & 2.5 & 2.7 & 2.9 & 2.8 \end{matrix}$$

$$\left. \begin{matrix} -4.9 & -4.1 & -3.5 \\ 2.7 & 2.5 & 1.8 \end{matrix} \right] 10^{-1} i \quad . \tag{36}$$

Again $[Y_{11}]^{-1}$ is calculated and Eq. (22) is used to calculate $[\phi_2]^T$. The mode shapes determined from the admittances in Eqs. (35) and (36) are compared to

Fig. 3. Experimentally determined first mode shape for the 6-ft beam structure compared with the first mode shape for a clamped-clamped continuum beam.

Fig. 4. Experimentally determined second mode shape for the 6-ft beam structure compared with the second mode shape for a clamped-clamped continuum beam.

TABLE 1

FIRST AND SECOND MODE DATA
FOR ADMITTANCES MEASURED AT 70 Hz

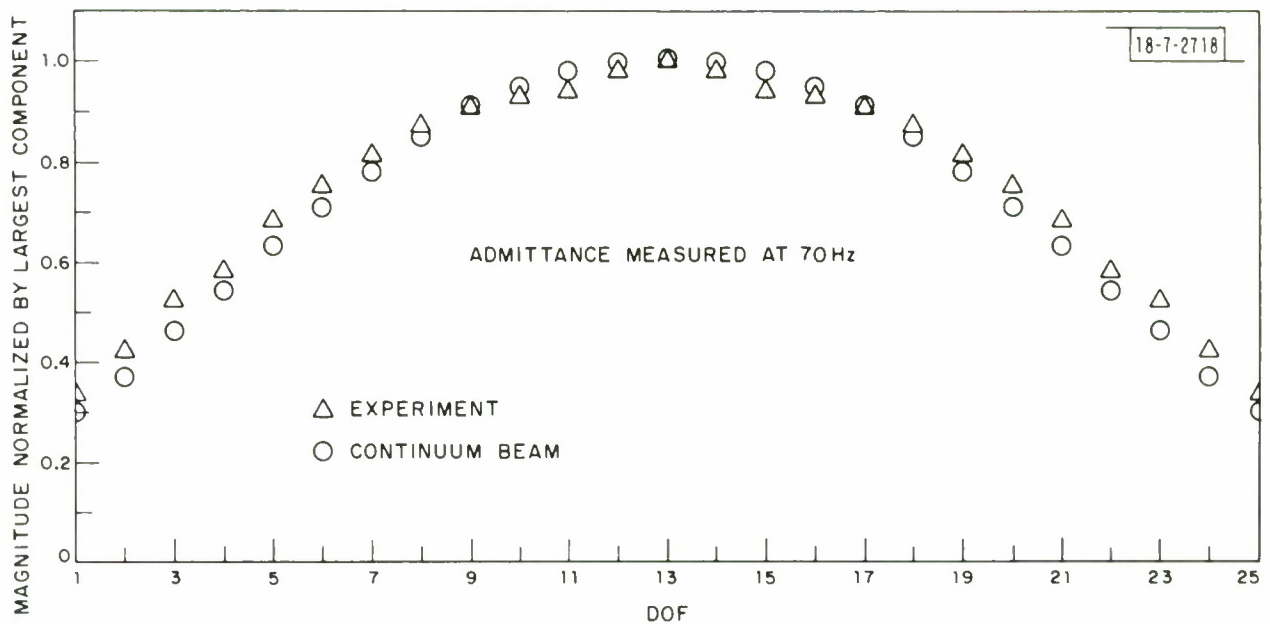| DOF	First Mode		Second Mode	
	Experiment	Continuum Beam	Experiment	Continuum Beam
1	0.33	0.30	0.7	0.66
2	0.42	0.37	0.8	0.77
3	0.52	0.46	0.9	0.89
4	0.58	0.54	1.0	0.96
5	0.68	0.63	1.0	0.99
6	0.75	0.71	0.9	1.00
7	0.81	0.78	1.0	0.95
8	0.87	0.85	1.0	0.87
9	0.91	0.91	1.0	0.75
10	0.93	0.95	0.7	0.58
11	0.94	0.98	0.6	0.40
12	0.98	1.00	0.2	0.23
13	1.00	1.00	0.0	0.00
14	0.98	1.00	−0.2	−0.23
15	0.94	0.98	−0.6	−0.40
16	0.93	0.95	−0.7	−0.58
17	0.91	0.91	−1.0	−0.75
18	0.87	0.85	−1.0	−0.87
19	0.81	0.78	−1.0	−0.95
20	0.75	0.71	−0.9	−1.00
21	0.68	0.63	−1.0	−0.99
22	0.58	0.54	−1.0	−0.96
23	0.52	0.46	−0.9	−0.89
24	0.42	0.37	−0.8	−0.77
25	0.33	0.30	−0.7	−0.66

Fig. 5. Experimentally determined first mode shape for the 6-ft beam structure compared with the first mode shape for a clamped-clamped continuum beam.
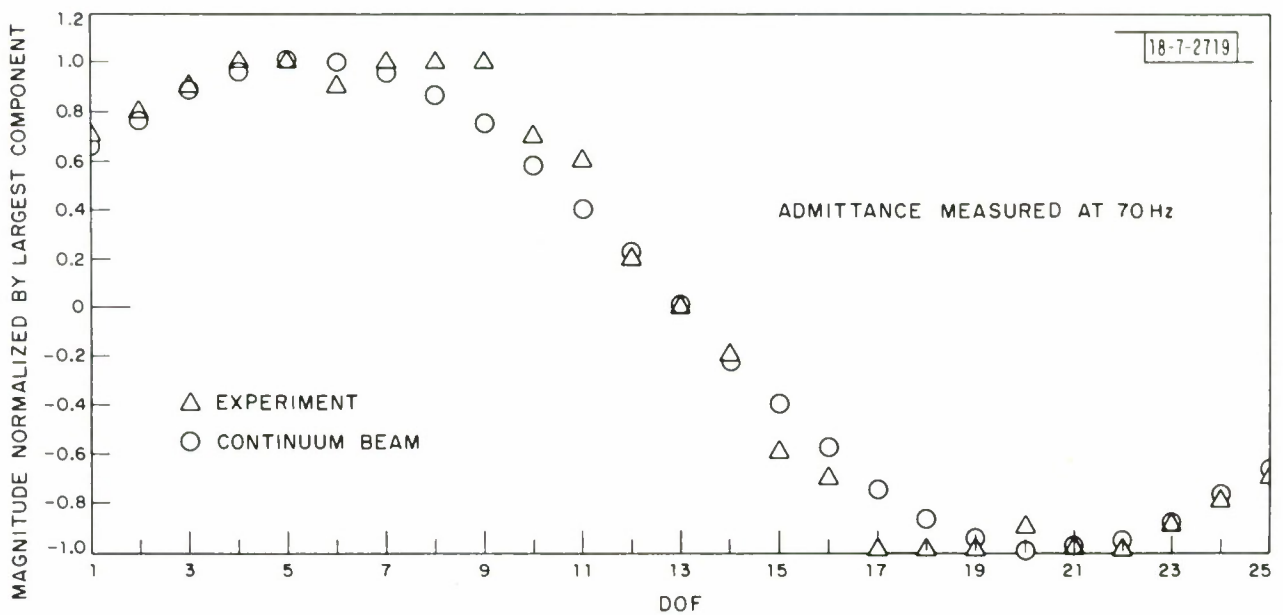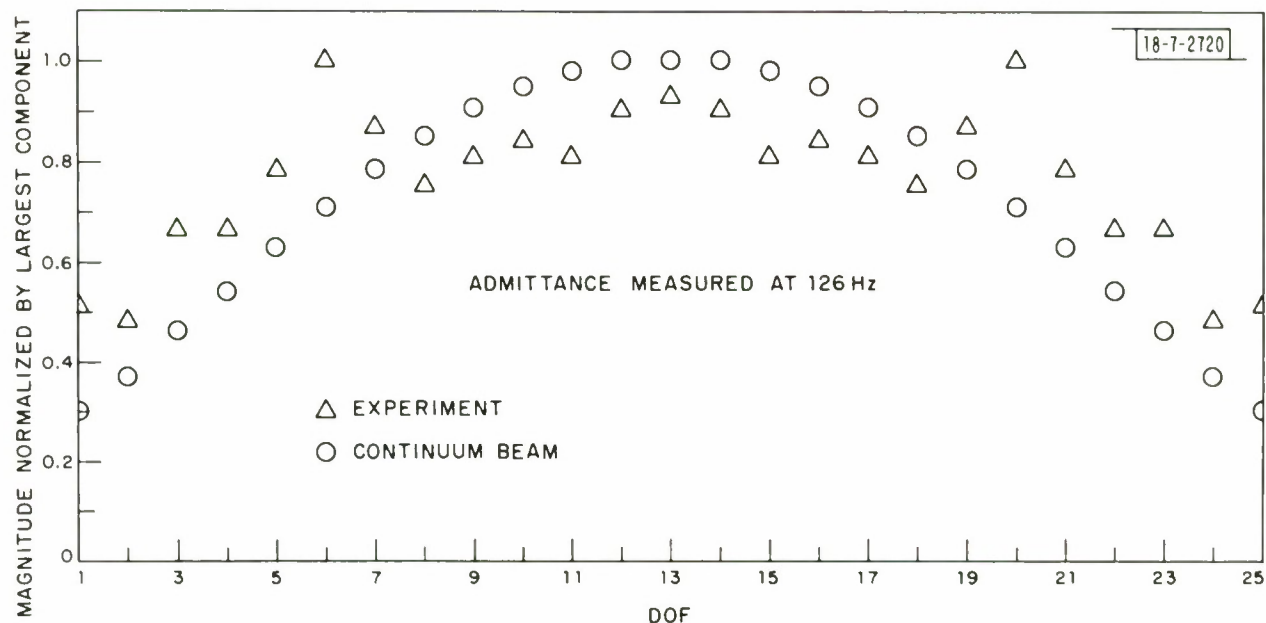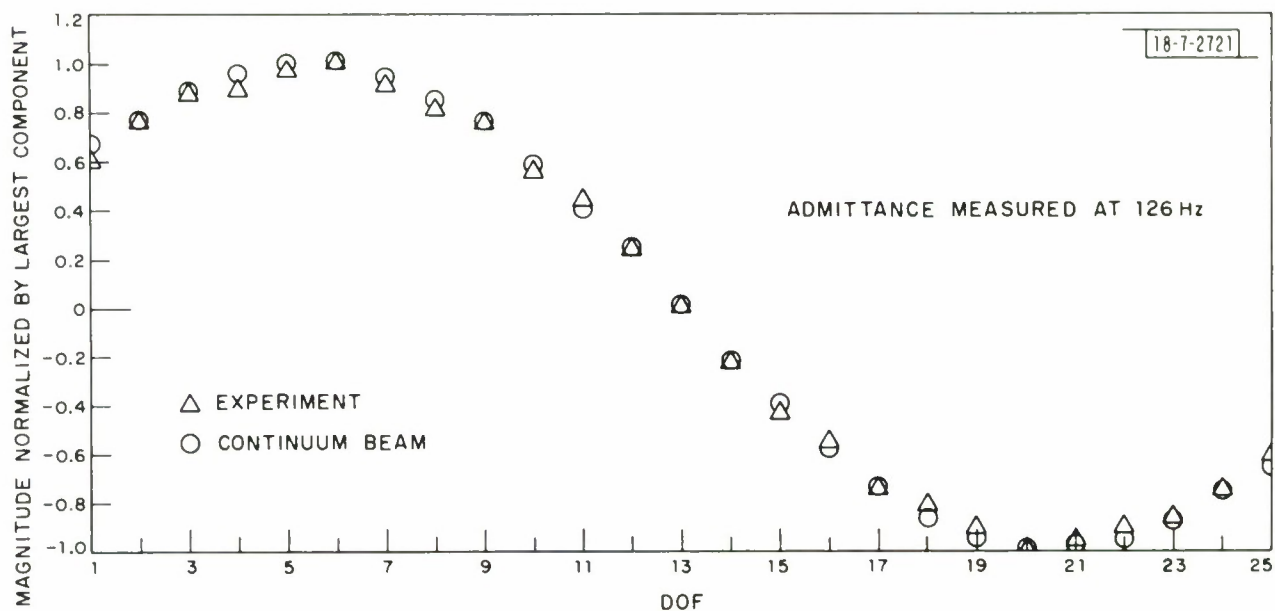

Fig. 6. Experimentally determined second mode shape for the 6-ft beam structure compared with the second mode shape for a clamped-clamped continuum beam.

the mode shapes of a clamped-clamped continuum beam (Figs. 5, 6 and Table 2). The second-mode shape is more accurate than the first-mode shape because the matrices $[Y_{11}]$ and $[Y_{21}]$ measured at 126 Hz are dominated by participation of the second mode.

One must ensure that participation of the mode shape to be calculated using Eq. (22) is large compared to the participation of the other mode shapes in $[Y_{11}]$ and $[Y_{21}]$. As a result, each mode shape of the structure should be calculated from values of $[Y_{11}]$ and $[Y_{21}]$ measured at a frequency of excitation relatively close to the mode shape's corresponding resonant frequency. The more accurate first-mode shape (Fig. 3) is calculated from data measured at 70 Hz, relatively close to the first resonant frequency observed in the measured admittances, 50 Hz. The more accurate second-mode shape (Fig. 6) is calculated from data measured at 126 Hz, relatively close to the second resonant frequency observed in the measured admittances, 138 Hz. However, choosing values of $[Y_{11}]$ and $[Y_{21}]$ at frequencies too close to the resonant frequencies can result in inaccurate mode shapes.

At and near resonant frequencies of the structure, the mechanical admittances are governed to a large degree by the damping. If the damping is significantly nonlinear, the mechanical admittances measured near resonant frequencies of the structure are not of the form shown in Eq. (37):

$$Y_{nj} = \sum_{\ell=1}^{\lambda} \frac{\frac{\omega}{m_\ell} \phi_n^\ell \phi_j^\ell}{i(\omega^2 - \omega_\ell^2) + D_\ell(\omega)} \quad . \tag{37}$$

Equation (37) is the expression for the nj^{th} admittance derived from Eq. (1). If an admittance of the structure, measured near a resonant frequency, cannot be modeled by Eq. (37), then the response of the structure cannot be modeled by Eq. (1) and the DE principle does not hold. If at frequencies of excitation away from resonant frequencies the contribution of the damping is relatively small, Eq. (38), the dynamic response of the structure can be modeled by Eq. (1) and the DE principle can be applied:

$$\left| (\omega^2 - \omega_\ell^2) \right| \gg \left| D_\ell(\omega) \right| \qquad \ell = 1, 2, 3 \ldots \lambda \quad . \tag{38}$$

15

TABLE 2

FIRST AND SECOND MODE DATA
FOR ADMITTANCES MEASURED AT 126 Hz

DOF	First Mode		Second Mode	
	Experiment	Continuum Beam	Experiment	Continuum Beam
1	0.51	0.30	0.61	0.66
2	0.48	0.37	0.76	0.77
3	0.66	0.46	0.87	0.89
4	0.66	0.54	0.89	0.96
5	0.78	0.63	0.97	0.99
6	1.00	0.71	1.00	1.00
7	0.87	0.78	0.91	0.95
8	0.75	0.85	0.81	0.87
9	0.81	0.91	0.75	0.75
10	0.84	0.95	0.55	0.58
11	0.81	0.98	0.44	0.40
12	0.90	1.00	0.23	0.23
13	0.93	1.00	0.00	0.00
14	0.90	1.00	−0.23	−0.23
15	0.81	0.98	−0.44	−0.40
16	0.84	0.95	−0.55	−0.58
17	0.81	0.91	−0.75	−0.75
18	0.75	0.85	−0.81	−0.87
19	0.87	0.78	−0.91	−0.95
20	1.00	0.71	−1.00	−1.00
21	0.78	0.63	−0.97	−0.99
22	0.66	0.54	−0.89	−0.96
23	0.66	0.46	−0.87	−0.89
24	0.48	0.37	−0.76	−0.77
25	0.51	0.30	−0.61	−0.66

If the damping is large and $[Y_{11}]$ and $[Y_{21}]$ cannot be measured at frequencies of excitation close enough to the resonant frequencies to calculate accurate mode shapes without the damping significantly distorting the admittances, there is an alternative.

The DE principle can be applied with less stringent restraints than Eq. (38) by ignoring completely the real part of the measured admittances. Equation (39) is Eq. (37) rewritten to separate the real and imaginary parts of the admittance:

$$Y_{nj} = \sum_{\ell=1}^{\lambda} \frac{\frac{\omega}{m_\ell} \phi_n^\ell \phi_j^\ell [-i(\omega^2 - \omega_\ell^2) + D_\ell(\omega)]}{(\omega^2 - \omega_\ell^2)^2 + D_\ell^2(\omega)} \tag{39}$$

$$Im(Y_{nj}) = \sum_{\ell=1}^{\lambda} \frac{\frac{\omega}{m_\ell} \phi_n^\ell \phi_j^\ell \, i(\omega_\ell^2 - \omega^2)}{(\omega^2 - \omega_\ell^2)^2 + D_\ell^2(\omega)} \, . \tag{40}$$

Equation (40) is the imaginary part of the admittance. If the conditions in Eq. (41) are met then Eq. (42) can be derived from Eq. (40):

$$(\omega^2 - \omega_\ell^2)^2 \gg D_\ell^2(\omega) \qquad \ell = 1, 2, 3 \ldots \lambda \tag{41}$$

$$Im(Y_{nj}) \approx \sum_{\ell=1}^{\lambda} \frac{\frac{i\omega}{m_\ell} \phi_n^\ell \phi_j^\ell}{(\omega_\ell^2 - \omega^2)} \, . \tag{42}$$

The conditions imposed on the choice frequencies of excitation where the admittances should be measured in Eq. (41) are less restrictive than the conditions imposed by Eq. (38). For instance, with the same damping, $D_\ell(\omega)$, the conditions in Eq. (41) allow one to choose frequencies of excitation, ω, closer to the resonant frequencies of the structure than does Eq. (38). Also for the same frequency of excitation, ω, Eq. (41) allows the damping, $D_\ell(\omega)$, to be larger than does Eq. (38).

Equation (42) indicates that as long as the conditions in Eq. (41) are met, the damping no longer significantly affects the imaginary part of the measured

17

admittances. As a result, the imaginary parts of measured admittances approximate the undamped admittances of the structure:

$$\text{Im}(Y_{nj}) \approx \sum_{\ell=1}^{\lambda} \frac{\frac{i\omega}{m_\ell} \phi_n^\ell \phi_j^\ell}{(\omega_\ell^2 - \omega^2)} = Y_{nj_{\text{undamped}}} \quad . \tag{43}$$

Only the imaginary parts of the measured admittances are used in calculations in this report.

Mechanical admittances measured close to resonant frequencies of the structure can be inaccurate for reasons other than damping. The mass of the shaker, the additional damping introduced by the shaker and the change in stiffness of the structure due to the attachment of the shaker have local maxima of their effects on measured admittances at resonant frequencies.[9] In addition, if the structure is suspended to simulate a free structure, the impedance of the suspension system has local maxima of its effects on measured admittances at resonant frequencies of the structure.[10]

By comparing the value of $[Y_{11}]^{-1} [Y_{21}]^T$ at 70 Hz vs the value of $[Y_{11}]^{-1} [Y_{21}]^T$ at 126 Hz it is apparent that $[Y_{11}]^{-1} [Y_{21}]^T$ is not invariant with respect to the frequency of excitation. This is because the structure has more than two mode shapes and corresponding resonant frequencies. The higher the frequency of excitation at which $[Y_{11}]$ and $[Y_{21}]$ are measured, the larger the participation of third and higher mode shapes in the measured admittances. By modeling the structure with more than two mode shapes, $[Y_{11}]^{-1} [Y_{21}]^T$ should be less sensitive to changes in the frequency of excitation within the $0 - 150$ Hz range.

This method of experimentally determining a structure's mode shapes has certain advantages over methods that attempt to excite and measure one mode shape of a structure at a time. First, less sophisticated equipment is required to measure an admittance than is necessary to produce a set of applied forces orthogonal to all but one mode shape of a structure. In addition, it is difficult to produce a set of applied forces that is orthogonal to all but one quasi-known mode shape of a structure.[11] Usually more than one mode shape is contributing

18

to the dynamic response of the structure even when excited at a resonant frequency. In cases where two or more resonant frequencies are very close together, it is extremely difficult to excite only one mode shape of the structure. The technique used to calculate the structure's mode shapes in this chapter assumes that λ mode shapes are participating in the structure's response over the entire frequency range of interest.

Finally, when attempting to excite only one mode shape of a structure one must excite the structure at a resonant frequency. The admittances dealt with in this section are not measured at resonant frequencies of the structure where the dynamic response of the structure is governed to a large degree by damping and affected by shakers and suspension systems.[12] These factors can distort the relative magnitudes and phases of the measured components of the structure's mode shapes.

CHAPTER III

EXPERIMENTAL GENERATION
OF MOMENT-ROTATIONAL VELOCITY IMPEDANCES

When assembling structures into a total structure using mechanical im-
pedance techniques, moment-rotational velocity impedances are required to
ensure the compatibility of rotational displacements at the interfaces of the
constituent structures. Usually it is impractical to measure impedances
directly from the structure due to the necessary boundary conditions that all
DOF except one must have zero velocity (displacement). It follows that one
should calculate the impedances from admittances measured on the structure.

To calculate moment-rotational velocity impedances it is necessary to
generate moment-rotational velocity admittances. In many situations, meas-
ured moment-rotational velocity admittances have eluded engineers due to the
difficulty in fabricating a shaker that applies a pure moment to a structure.

The DE principle can be used to circumvent this problem. The structure
is assumed to have λ mode shapes and L DOF, $L > \lambda$. The structure's DOF
are divided into two subsets, λ linear DOF in the first subset and $L-\lambda$ rotation
DOF in the second subset. Equation (25) can be used to calculate moment-
rotational velocity admittances, $[Y_{22}]$, from force-velocity admittances, $[Y_{11}]$,
and force-rotational velocity admittances, $[Y_{21}]$. Then one could calculate
the moment-rotational velocity impedances, $[Z_{22}]$, from $[Y_{22}]$.

This method of calculating the moment-rotational velocity impedances,
although straightforward, has many shortcomings. First, one must be able
to measure accurately all the admittances, $[Y_{11}]$ and $[Y_{21}]$, over the entire
frequency range of interest. As seen in the last chapter, admittances can be
distorted near resonant frequencies by damping. Other errors can be intro-
duced near resonant frequencies by shakers and suspension systems. In
addition, the frequency range of the measuring equipment may not cover the
entire frequency range of interest. Second, if the order of $[Y_{22}]$ is greater
than λ, the inverse of $[Y_{22}]$, $[Z_{22}]$, does not exist because there are only λ
linearly independent mode shapes of the structure. The third major short-
coming is the large amount of data that must be processed to calculate $[Z_{22}]$
at all the necessary frequencies.

20

It is more efficient to solve for two invariant matrices of the structure, the mass matrix and stiffness matrix, and use them to calculate an impedance matrix containing moment-rotational velocity impedances:

$$[Z] = i\omega [M] + (i\omega)^{-1} [K] \quad . \tag{44}$$

Initially, one calculates the mass matrix and stiffness matrix using the inverse eigenvalue method from the admittances measured at the structure's first DOF subset.[13] Since the mass matrix, $[M_{11}]$, and the stiffness matrix, $[K_{11}]$, are calculated from admittances measured only at the subset of DOF, the mass matrix and stiffness matrix characterize the behavior of the structure only at its first DOF subset.

The mode shapes at the first DOF subset, $\{\phi_1^\ell\}$, and resonant frequencies of the structure, ω_ℓ, are calculated from the mass matrix and stiffness matrix using the iterative method.[14]

$$\{0\} = -\omega_\ell^2 [M_{11}] \{\phi_1^\ell\} + [K_{11}] \{\phi_1^\ell\} \qquad \ell = 1, 2, 3 \ldots \lambda \tag{45}$$

$$\lfloor \phi_1^\ell \rfloor [M_{11}] \{\phi_1^\ell\} = m_\ell \qquad \ell = 1, 2, 3 \ldots \lambda \tag{46}$$

$$\{\phi_1^\ell\} \frac{1}{\sqrt{m_\ell}} = \left\{ \frac{\phi_1^\ell}{\mu_\ell} \right\} \quad ; \quad \mu_\ell = \sqrt{m_\ell} \qquad \ell = 1, 2, 3 \ldots \lambda \tag{47}$$

where

$\omega_\ell = \ell^{th}$ resonant frequency in radians per second

$m_\ell = \ell^{th}$ modal mass

$\{\phi_1^\ell\} = \ell^{th}$ unnormalized mode shape for the first DOF subset

$\left\{ \dfrac{\phi_1^\ell}{\mu_\ell} \right\} = \ell^{th}$ normalized mode shape for the first DOF subset.

The normalized mode shape at the first DOF subset are assembled into a normalized modal matrix of the structure:

$$\left[\left\{\frac{\phi_1^1}{\mu_1}\right\}\ \left\{\frac{\phi_1^2}{\mu_2}\right\}\ \left\{\frac{\phi_1^3}{\mu_3}\right\}\cdots\left\{\frac{\phi_1^\lambda}{\mu_\lambda}\right\}\right] = \left[\frac{\phi_1}{\mu}\right] \qquad . \tag{48}$$

$[\phi_1/\mu]$, the normalized modal matrix for the first DOF subset, and $[Y_{11}]$ and $[Y_{21}]$ measured in the vicinity of each resonant frequency are sufficient to calculate $[\phi_2/\mu]$, the normalized modal matrix for the second DOF subset using Eq. (49):

$$\left[\frac{\phi_2}{\mu}\right]^T = \left[\frac{\phi_1}{\mu}\right]^T [Y_{11}]^{-1} [Y_{21}]^T \qquad . \tag{49}$$

Equation (49) is derived from Eq. (22) in Chap. I:

$$[\phi_2]^T = [\phi_1]^T [Y_{11}]^{-1} [Y_{21}]^T \qquad . \tag{22}$$

The normalized mode shapes of the structure are determined at both DOF subsets and are used to construct the total normalized mode shapes of the structure: .

$$\left\{\frac{\phi^\ell}{\mu_\ell}\right\} = \left\{\begin{array}{c}\dfrac{\phi_1^\ell}{\mu_\ell}\\ \hline \dfrac{\phi_2^\ell}{\mu_\ell}\end{array}\right\} \qquad \ell = 1, 2, 3\ldots\lambda \qquad . \tag{50}$$

λ components, chosen from each total normalized mode shape, are used to construct each reduced mode shape, $\{\phi_3^\ell/\mu_\ell\}$. The impedances to be calculated from $\{\phi_3^\ell/\mu_\ell\}$ will be used to ensure the compatibility of displacement at the interfaces of the structure with other structures. As a result the λ components of $\{\phi_3^\ell/\mu_\ell\}$ must represent at least all the rotational and linear DOFs on the interfaces of the structure.

The reduced normalized mode shapes of the structure, $[\phi_3/\mu]$ and the structure's resonant frequencies, ω_ℓ, are used to calculate mass and stiffness

matrices representing the DOF at the interfaces of the structure.

$$
\begin{bmatrix}
\omega_1^2 & & & & & & 0 \\
& \omega_2^2 & & & & & \\
& & \omega_3^2 & & & & \\
& & & \ddots & & & \\
& & & & \ddots & & \\
& & & & & \ddots & \\
0 & & & & & & \omega_\lambda^2
\end{bmatrix} = [\omega_\lambda^2] \quad . \tag{51}
$$

The relationships of the mass matrix and stiffness matrix of a structure to its normalized mode shapes and resonant frequencies are given in Eqs. (52) and (53):

$$
\left[\frac{\phi_3}{\mu}\right]^T [K_{33}] \left[\frac{\phi_3}{\mu}\right] = [\omega_\lambda^2] \tag{52}
$$

$$
\left[\frac{\phi_3}{\mu}\right]^T [M_{33}] \left[\frac{\phi_3}{\mu}\right] = [I] \quad . \tag{53}
$$

Premultiplying both sides of Eqs. (52) and (53) by $[\phi_3/\mu]^{T-1}$ and postmultiplying both sides of both equations by $[\phi_3/\mu]^{-1}$ produces Eqs. (54) and (55):

$$
[K_{33}] = \left[\frac{\phi_3}{\mu}\right]^{T-1} [\omega_\lambda^2] \left[\frac{\phi_3}{\mu}\right]^{-1} \tag{54}
$$

$$
[M_{33}] = \left[\frac{\phi_3}{\mu}\right]^{T-1} \left[\frac{\phi_3}{\mu}\right]^{-1} \tag{55}
$$

Equations (54) and (55) show that the structure must have at least as many linearly independent mode shapes as there are DOF at its interfaces or else $[\phi_3/\mu]^{T-1}$ and $[\phi_3/\mu]^{-1}$ do not exist. If $[\phi_3/\mu]^{T-1}$ and $[\phi_3/\mu]^{-1}$ do not exist,

23

Eqs. (54) and (55) cannot be used to calculate the structure's mass matrix and stiffness matrix. Using Eqs. (54) and (55) one can solve for the mass matrix and stiffness matrix of the structure representing its DOF at its interfaces.

Using the relationship in Eq. (56) the corresponding impedance matrix can be constructed:

$$[Z_{33}] = i\omega [M_{33}] + (i\omega)^{-1} [K_{33}] \quad . \tag{56}$$

Conventional impedance techniques can now be applied to assemble analytically this structure to other structures ensuring the compatibility of linear and rotational displacement at the interfaces.

CHAPTER IV
COUPLING TWO BEAM STRUCTURES
USING EXPERIMENTALLY GENERATED IMPEDANCES

The 6-ft aluminum clamped-clamped beam structure dealt with in Chap. II is cut in half. The two halves of the 6-ft beam structure are reassembled analytically using impedances generated experimentally as shown in Chap. III. The analytically reassembled beam structure's resonant frequencies and mode shapes are compared with the resonant frequencies and mode shapes generated for the 6-ft beam structure in Chap. II. The mode shapes and resonant frequencies of a similar continuum beam are also shown for comparison.

Both halves of the 6-ft beam structure are modeled as clamped-free beam structures, each with three DOF, $L = 3$ (Fig. 7).
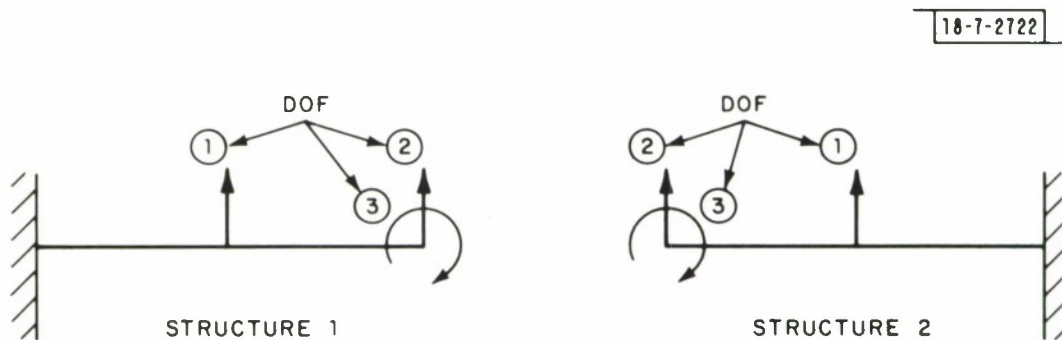

Fig. 7. Two clamped-free beam structures.

Admittances are measured with equipment (Fig. 2) described in Chap. II at the DOF of structure 1 in Fig. 7. (Due to the similarity of structures 1 and 2, admittance measurements are made only on structure 1. The impedances of structure 1 are determined as shown in Chap. III; impedances for structure 2 are constructed from impedances of structure 1 by inspection.) The actual clamped-free beam with shaker/impedance head attached (Fig. 8) is separated from its support by a steel plate at the base of the clamped-free beam. The beam tilts to the right to provide room for the accelerometer that measures the response at the rotational DOF.

Fig. 8. Three-ft, clamped-free beam structure with shaker/impedance head attached.
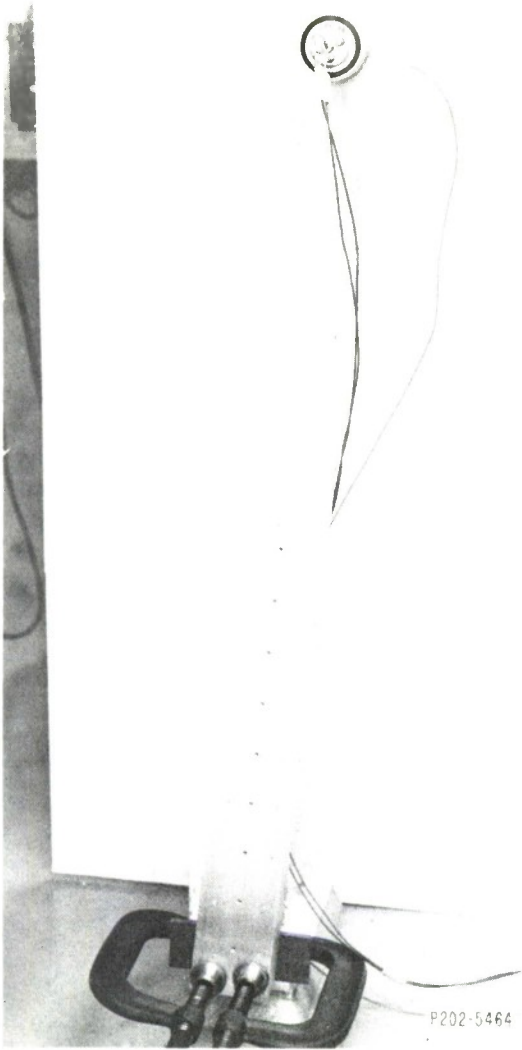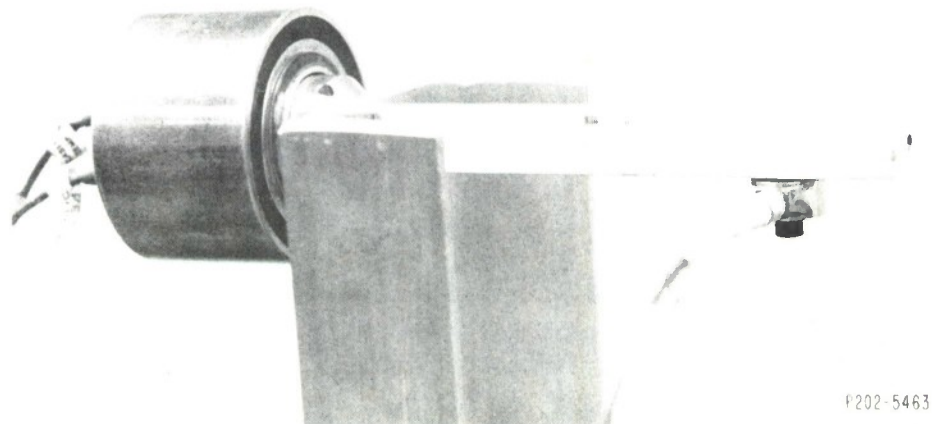
P202-5464

Fig. 9. Lever arm, accelerometer and shaker/impedance head measuring cross-admittances for the rotational DOF of structure 1.

P202-5463

The dynamic response at the rotational DOF of the structure is measured by an accelerometer mounted on a lever arm to detect changes in the slope of the free end of the beam (Fig. 9). For small rotations the rotation of the free end of the beam in radians is equal to the slope at the end of the beam:

$$\frac{dy}{dx} = \Theta \tag{57}$$

$$\frac{d\dot{y}}{dx} = \dot{\Theta} \tag{58}$$

$$\frac{\dot{y}}{R} = \dot{\Theta} \tag{59}$$

$$\frac{\dot{y}}{fR} = \frac{\dot{\Theta}}{f} \tag{60}$$

$$Y/R = Y_\Theta \quad . \tag{61}$$

Equation (61) shows that the force-linear velocity cross-admittance measured at DOF 3 divided by the length of the lever arm, R, is equal to the force-rotational velocity admittance of the free end of the beam.

This relationship, Eq. (61), is invalid if there is any significant axial motion of the beam. The shaker/impedance head is attached only at DOFs 1 and 2 making the applied forces orthogonal to the axial modes of the beam. In addition, the locations and direction of the applied forces are chosen such that torsional motion of the beam is not produced.

The low frequency dynamic behavior of structure 1, less than 200 Hz, is dominated by two mode shapes. These mode shapes correspond to two resonant frequencies below 200 Hz. The third resonant frequency of the structure is approximately 500 Hz. The modal participation coefficient of the third mode is considered small compared to the modal participation coefficients of the first two modes for frequencies of excitation less than 200 Hz. For low frequencies of excitation the structure is assumed to have only two resonant frequencies and two mode shapes, $\lambda = 2$, while the structure has three DOF, $L = 3$.

The first DOF subset is DOFs 1 and 2 and the second subset is DOF 3. The mutual and cross-admittances measured at the first DOF subset are used

27

to calculate the structure's mass matrix and stiffness matrix.[15] This mass matrix and stiffness matrix characterize the behavior of the structure only at its first DOF subset:

$$[K_{11}]_1 = \begin{bmatrix} 2.96 & -1.03 \\ -1.03 & 0.43 \end{bmatrix} 10^3 \text{ lb/in.} \tag{62}$$

$$[M_{11}]_1 = \begin{bmatrix} 4.71 & 0.70 \\ 0.65 & 1.70 \end{bmatrix} 10^{-3} \text{ slug} \quad . \tag{63}$$

The structure's resonant frequencies, modal masses and normalized mode shapes for the first DOF subset are calculated from the mass and stiffness matrices using the iterative method.[16] The results are given in Table 3.

TABLE 3

RESONANT FREQUENCIES, MODAL MASSES
AND NORMALIZED MODE SHAPES FOR STRUCTURE 1

$\nu_1 = \dfrac{\omega_1}{2\pi} = 25.8 \text{ Hz}$	$m_1 = 2.84 \times 10^{-3} \text{ slug}$	$\left\{ \dfrac{\phi_1^1}{\mu_1} \right\}_1 = \left\{ \begin{matrix} 6.9 \\ 18.8 \end{matrix} \right\}$
$\nu_2 = \dfrac{\omega_2}{2\pi} = 167 \text{ Hz}$	$m_2 = 3.76 \times 10^{-3} \text{ slug}$	$\left\{ \dfrac{\phi_1^2}{\mu_2} \right\}_1 = \left\{ \begin{matrix} -13.4 \\ 16.3 \end{matrix} \right\}$

The normalized mode shapes at the first DOF subset, $[\phi_1/\mu]$, and the admittance matrices $[Y_{11}]$ and $[Y_{21}]$ measured at 40 Hz and Eq. (49) are used to solve for structure 1's normalized mode shapes at the second DOF subset, $[\phi_2/\mu]$:

$$\left[\frac{\phi_2}{\mu}\right]^T = \left[\frac{\phi_1}{\mu}\right]^T [Y_{11}]^{-1} [Y_{21}]^T \tag{49}$$

$$\left[\frac{\phi_2}{\mu}\right]_1^T = \begin{bmatrix} 6.9 & 18.8 \\ -13.4 & 16.3 \end{bmatrix} \begin{bmatrix} -10.86 & 4.36 \\ 4.36 & -1.33 \end{bmatrix} i \begin{bmatrix} 3.25 \\ 6.01 \end{bmatrix} 10^{-2} i = \begin{bmatrix} -0.585 \\ -2.23 \end{bmatrix} . \quad (64)$$

The reduced mode shapes, $\{\phi_3^\ell/\mu\}$, are constructed using components from DOFs 2 and 3 and are shown in Table 4.

<div align="center">

TABLE 4

REDUCED MODE SHAPES OF STRUCTURE 1

$$\left\{\frac{\phi_3^1}{\mu_1}\right\}_1 = \left\{\begin{matrix} 18.8 \\ -0.585 \end{matrix}\right\} \quad \left\{\frac{\phi_3^2}{\mu_2}\right\}_1 = \left\{\begin{matrix} 16.3 \\ -2.23 \end{matrix}\right\}$$

</div>

Both DOF at the interface of structure 1 with structure 2 are accounted for in the reduced mode shape. As a result, compatibility of lateral and rotational displacement at the interface is assured when the two structures are assembled using impedance techniques.

The reduced mode shapes, $[\phi_3/\mu]_1$, the structure's resonant frequencies and modal masses calculated above are

18-7-2723

Fig. 10. Structure 1 using DOFs 2 and 3.

used to calculate the mass and stiffness matrices of structure 1 (Fig. 10). The mass and stiffness matrices are calculated using Eqs. (54) and (55) and are shown in Eqs. (65) and (66):

$$[K_{33}] = \left[\frac{\phi_3}{\mu}\right]^{T-1} [\omega_\ell^2] \left[\frac{\phi_3}{\mu}\right]^{-1} \quad (54)$$

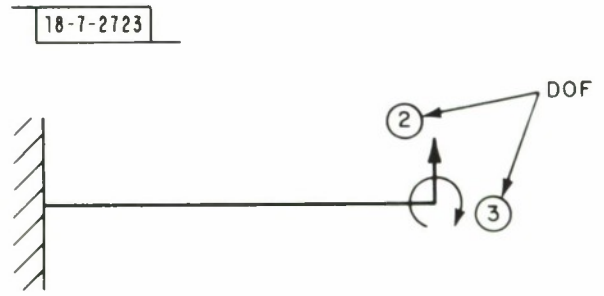$$[M_{33}] = \left[\frac{\phi_3}{\mu}\right]^{T-1} \left[\frac{\phi_3}{\mu}\right]^{-1} \quad (55)$$

$$[K_{33}]_1 = \begin{bmatrix} 0.466 & 12.1 \\ 12.1 & 374 \end{bmatrix} 10^3 \tag{65}$$

$$[M_{33}]_1 = \begin{bmatrix} 4.73 & 44.4 \\ 44.4 & 586 \end{bmatrix} 10^{-3} \quad . \tag{66}$$

The mass matrix, Eq. (66), is corrected for the 0.27×10^{-3} slug mass of the lever arm in Fig. 9. Its rotary inertia is negligible.

The mass and stiffness matrices are used to construct the impedance matrix of the structure in Fig. 10:

$$[Z_{33}] = i\omega [M_{33}] + (i\omega)^{-1} [K_{33}] \quad . \tag{56}$$

By changing the sign of the appropriate elements in $[K_{33}]_1$ and $[M_{33}]_1$ one can produce the mass matrix, stiffness matrix and impedance matrix of structure 2 (Fig. 11).
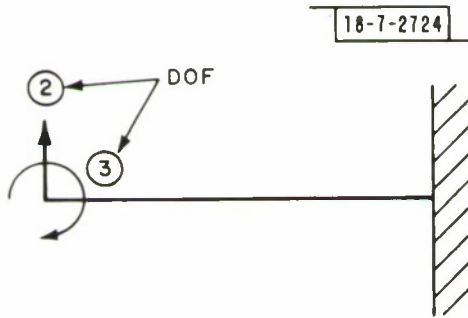

Fig. 11. Structure 2 modeled with two DOF.

The mass matrix, $[M_{33}]_2$, and the stiffness matrix, $[K_{11}]_2$, of structure 2 are given in Eqs. (67) and (68):

$$[K_{33}]_2 = \begin{bmatrix} 0.466 & -12.1 \\ -12.1 & 374 \end{bmatrix} 10^3 \tag{67}$$

$$[M_{33}]_2 = \begin{bmatrix} 4.73 & -44.4 \\ -44.4 & 586 \end{bmatrix} 10^{-3} \tag{68}$$

$$[Z_{33}]_2 = i\omega \, [M_{33}]_2 + (i\omega)^{-1} \, [K_{33}]_2 \quad . \tag{69}$$

Using conventional impedance techniques the structure in Fig. 10 is coupled to the structure in Fig. 11. The resultant structure is a 6-ft clamped-clamped beam structure. The impedance matrix of the total structure $[Z]_T$ is determined using Eq. (70):

$$[Z]_T = [Z_{33}]_1 + [Z_{33}]_2 = i\omega \left[[M_{33}]_1 + [M_{33}]_2 \right]$$

$$+ (i\omega)^{-1} \left[[K_{33}]_1 + [K_{33}]_2 \right] \tag{70}$$

$$[K]_T = [K_{33}]_1 + [K_{33}]_2 = \begin{bmatrix} 0.932 & 0 \\ 0 & 748 \end{bmatrix} 10^3 \tag{71}$$

$$[M]_T = [M_{33}]_1 + [M_{33}]_2 = \begin{bmatrix} 0.946 & 0 \\ 0 & 117 \end{bmatrix} 10^{-2} \quad . \tag{72}$$
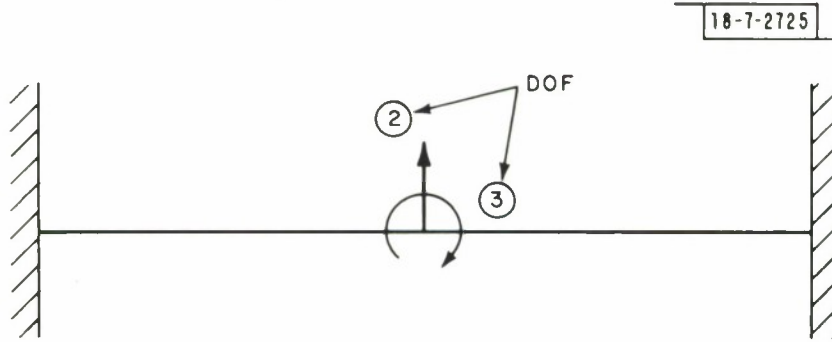
18-7-2725

Fig. 12.   Total beam structure.

The total structure's resonant frequencies and normalized mode shapes are calculated from the mass matrix, $[M]_T$, and stiffness matrix, $[K]_T$. The resonant frequencies of the 6-ft clamped beam structure calculated in this chapter are compared in Table 5 to the resonant peaks observed in the admittances measured for Chap. II, the resonant frequencies calculated in Chap. II and the resonant frequencies of a 6-ft clamped-clamped continuum beam.

31

TABLE 5

COMPARISON OF RESONANT FREQUENCIES FOR 6-FT DOUBLE-CLAMPED BEAMS

Observed Resonant Peaks (Chap. II):	$\nu_1 = 50.0$ Hz $\nu_2 = 138.0$ Hz	Continuum Beam:	$\nu_1 = 55.3$ Hz $\nu_2 = 152.0$ Hz
Calculated in Chap. II:	$\nu_1 = 53.2$ Hz $\nu_2 = 139.0$ Hz	Calculated in Chap. IV:	$\nu_1 = 50.0$ Hz $\nu_2 = 127.0$ Hz

The second resonant frequency calculated from the experimentally generated impedances is relatively inaccurate compared to the values determined for the second resonant frequency in Chap. II. The accuracy of the second calculated resonant frequency might be improved if a more accurate component of the second-mode shape of structure 1 at DOF 3 were calculated. The component of the second-mode shape of structure 1 at DOF 3 is calculated using Eq. (49). The admittance matrices $[Y_{11}]$ and $[Y_{21}]$ used in Eq. 49 are measured at 40 Hz, which is relatively close to the first resonant frequency and relatively far from the second resonant frequency of structure 1. As a result the participation of the second mode is far less than the participation of the first mode in $[Y_{11}]$ and $[Y_{21}]$. Under these conditions one would expect to calculate the components of the second-mode shape with less accuracy than the components of the first-mode shape. It is not possible to calculate the component of the second-mode shape of structure 1 at DOF 3 with data measured closer to the second resonant frequency due to significant elastic motion of the lever arm (Fig. 9) at frequencies above 40 Hz.

If resonant frequencies calculated for the total structure are not in the frequency range where the λ mode shapes dominate structure 1 or structure 2's response, the calculated resonant frequencies and corresponding mode shapes are probably inaccurate. The assumption at the beginning of this chapter, that the dynamic behavior of structures 1 and 2 is dominated by their first two modes, is not valid at frequencies above 200 Hz. If resonant frequencies and mode shapes of the total structure above 200 Hz are desired,

then one must characterize structures 1 and 2 with additional mode shapes and DOF to accurately model their dynamic behavior above 200 Hz.

The mass matrix, $[M]_T$, and stiffness matrix, $[K]_T$, of the total structure, Eqs. (71) and (72), are relatively accurate compared to the mass matrix and stiffness matrix of a 6-ft clamped continuum beam, Eqs. (73) and (74). (The methods used to construct Eqs. (73) and (74) are discussed in the Appendix.)

$$[K]_T = \begin{bmatrix} 0.932 & 0 \\ 0 & 748 \end{bmatrix} 10^3 \tag{71}$$

$$[M]_T = \begin{bmatrix} 0.946 & 0 \\ 0 & 117 \end{bmatrix} 10^{-2} \tag{72}$$

$$[K]_T \text{ continuum beam} = \begin{bmatrix} 1.28 & 0 \\ 0 & 969 \end{bmatrix} 10^3 \tag{73}$$

$$[M]_T \text{ continuum beam} = \begin{bmatrix} 1.06 & 0 \\ 0 & 106 \end{bmatrix} 10^{-2} . \tag{74}$$

The normalized mode shapes of the total structure calculated from the total structure's mass matrix, $[M]_T$, and stiffness matrix, $[K]_T$ are given in Table 6.

TABLE 6

NORMALIZED MODE SHAPES OF THE TOTAL STRUCTURE

$$\left| \frac{\phi^1}{\mu_1} \right|_T = \begin{Bmatrix} 10.3 \\ 0 \end{Bmatrix} \qquad \left| \frac{\phi^2}{\mu_2} \right|_T = \begin{Bmatrix} 0 \\ 0.93 \end{Bmatrix}$$

Unfortunately the mode shapes in Table 6 include only the DOF of the total structure encompassed by the reduced mode shapes of the constituent substructures. These DOF are shown in Fig. 12. The DOF at midspan of structure 1 and structure 2 (Fig. 7) are not accounted for in the mode shapes in Table 6. These interior DOF are not included in the reduced mode shapes of their respective substructures.

Assume that the total structure is in steady-state free (no applied forces) motion proportional to only one of its mode shapes:

$$\{x\} = c \left| \frac{\phi^n}{\mu_n} \right|_T \quad . \tag{75}$$

The displacements at the boundaries of each substructure are known. Focusing attention on one substructure, Eq. (75) is rewritten to include only the DOF at the substructure's boundaries. These DOF are also the DOF included in the reduced mode shapes of the substructure, Eq. (76):

$$\{x_3\} = c \left| \frac{\phi^n}{\mu_n} \right|_{T_3} \quad . \tag{76}$$

The displacements on the boundary of the substructure, $\{x_3\}$, can also be expressed as a linear combination of the substructure's mode shapes:

$$\{x_3\} = \left| \frac{\phi_3}{\mu} \right| \{a\} \quad . \tag{77}$$

Since there are λ DOF on the boundary of the substructure where the displacement is known and there are λ, linearly independent, reduced-mode shapes for the substructure, there exists a unique solution, $\{a\}$, to Eq. (77):

$$\left| \frac{\phi_3}{\mu} \right|^{-1} \{x_3\} = \{a\} \quad . \tag{78}$$

Using Eqs. (76) and (78), one can relate the components of the total structure's mode shape at the boundaries of the substructure to the reduced mode shapes of the substructure:

34

$$c \left[\frac{\phi_3}{\mu}\right]^{-1} \left\{\frac{\phi^n}{\mu_n}\right\}_{T_3} = \{a\} \quad .$$ (79)

All the quantities on the left-hand side of Eq. (79) are known, therefore $\{a\}$ is determined.

Since the modal participation of the reduced-mode shapes $\{a\}$ of the substructure is determined and the components of the substructure's mode shapes at its interior DOF were previously determined, Table 3, one can solve for the motion of the substructure at its interior DOF:

$$\{x_I\} = \left[\frac{\phi_I}{\mu}\right] \{a\} \quad .$$ (80)

The initial assumption for this derivation is that the total structure's motion is proportional to one of its mode shapes. Therefore $\{x_I\}$ is proportional to the total structure's mode shape at the DOF in the interior of the substructure:

$$\{x_I\} = c \left\{\frac{\phi^n}{\mu_n}\right\}_{T_I} \quad .$$ (81)

Using Eqs. (79), (80) and (81) the components of the total structure's mode at the DOF in the interior of the substructure are determined:

$$\left\{\frac{\phi^n}{\mu_n}\right\}_{T_I} = \left[\frac{\phi_I}{\mu}\right] \left[\frac{\phi_3}{\mu}\right]^{-1} \left\{\frac{\phi^n}{\mu_n}\right\}_{T_3}$$ (82)

The complete mode shapes for the total structure shown in Fig. 13 are calculated and given in Table 7.

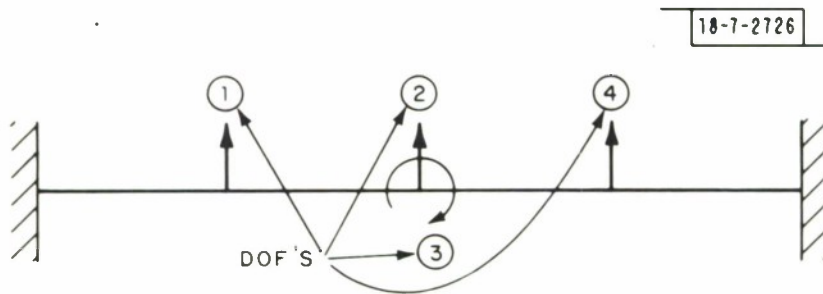Fig. 13. Total beam structure with all DOF.

TABLE 7

COMPLETE MODE SHAPES
FOR THE TOTAL BEAM STRUCTURE

$$\left|\frac{\phi^1}{\mu_1}\right|_T = \left\{\begin{array}{c} 7.3 \\ 10.3 \\ 0.0 \\ 7.3 \end{array}\right\} \qquad \left|\frac{\phi^2}{\mu_2}\right|_T = \left\{\begin{array}{c} 10.4 \\ 0.0 \\ 0.93 \\ -10.4 \end{array}\right\}$$

For comparison, the normalized mode shapes of the 6-ft clamped-clamped beam structure determined in Chap. II are given in Table 8. Table 9 shows the normalized mode shapes of a 6-ft clamped-clamped continuum beam.

TABLE 8

NORMALIZED MODE SHAPES FOR THE 6-FT BEAM
STRUCTURE DETERMINED IN CHAPTER II

$$\left|\frac{\phi_1}{\mu_1}\right| = \left\{\begin{array}{c} 5.6 \\ 9.8 \\ 0.0 \\ 5.6 \end{array}\right\} \qquad \left|\frac{\phi_2}{\mu_2}\right| = \left\{\begin{array}{c} 10.4 \\ 0.0 \\ 0.73 \\ -10.4 \end{array}\right\}$$

TABLE 9

NORMALIZED MODE SHAPES FOR A 6-FT
CLAMPED-CLAMPED CONTINUUM BEAM

$$\left|\frac{\phi_1}{\mu_1}\right| = \left\{\begin{array}{c} 5.2 \\ 9.7 \\ 0.0 \\ 5.2 \end{array}\right\} \qquad \left|\frac{\phi_2}{\mu_2}\right| = \left\{\begin{array}{c} 8.8 \\ 0.0 \\ 0.97 \\ -8.8 \end{array}\right\}$$

OVERVIEW AND CONCLUSIONS

The principle of dynamic equipollency coupled with the inverse eigenvalue method can overcome two weak areas of mechanical admittance/impedance testing. The principle makes possible the generation of moment-rotational velocity admittances and impedances from experimental data as well as the efficient treatment of structures having many DOF.

When solving for a mode shape of a structure having many DOF it is necessary to take admittance measurements relatively close to the resonant frequency corresponding to the mode shape in question. This ensures a relatively large participation of the mode shape in the measured admittances. It should be kept in mind, however, that admittance measurements taken too close to a resonant frequency may be distorted by nonlinear damping, the effects of the shaker and/or the effects of a suspension system.

The experimental generation of moment-rotational velocity admittances and impedances makes possible the assembling of substructures into a total structure ensuring the compatibility of rotational as well as lateral displacements at the interfaces. The only significant restraint on using the DE principle to accomplish this is that each substructure must have at least as many mode shapes (elastic and rigid body) as it has DOFs at its boundaries.

APPENDIX
CHARACTERISTICS OF CONTINUUM BEAMS

Throughout this report the experimentally determined characteristics of the beam structures are compared to the characteristics of similar continuum beams. This section deals with the methods used to calculate the characteristics of the continuum beams.

The mode shapes of the continuum beams are lifted directly from tables[17] and are normalized in a manner similar to the experimentally determined mode shapes with which they are compared. The resonant frequencies of the continuum beams are calculated using Eq. (A-1):[18]

$$\omega_n = \beta_n^2 \sqrt{EI/\rho} \qquad (A-1)$$

where

ω_n = nth resonant frequency expressed in radians per second

E = Young's Modulus for aluminum = 9.67×10^6 psi

I = second moment of area of the cross section of the beam = 0.25 in.^{4}

ρ = mass per unit length of the beams = 3.74×10^{-4} slug/in.

β_n = parameter based on length of the beam and displacement boundary conditions, i.e., clamped-clamped, clamped-free, etc.[19]

The stiffness matrices of the continuum beams are calculated using Eq. (A-2):

$$[K] = [\tfrac{\phi}{\mu}]^{T-1} [\omega_n^2] [\tfrac{\phi}{\mu}]^{-1} \qquad (A-2)$$

38

where

$[\omega_n^2]$ = diagonal matrix containing the resonant frequencies
corresponding to the mode shapes in $[\phi/\mu]$

$[\phi/\mu]$ = normalized modal matrix of the continuum beam and
contains a finite number of mode shapes.

This represents the assumption that the low frequency dynamic behavior of
the continuum beam can be approximated by its first two mode shapes. The
mode shapes in $[\phi/\mu]$ correspond to the λ mode shapes of the beam structure
being compared to the continuum beam.

Each mode shape in $[\phi/\mu]$ is normalized by the square root of its respective
modal mass. The modal mass of the continuum beams are calculated using
Eq. (A-3):

$$\rho \ell = m_n \quad . \tag{A-3}$$

where

m_n = modal mass

ℓ = length of the beam

ρ = mass per unit length.

The tabulated mode shapes for the continuum beams[20] are normalized
using Eq. (A-4):[21]

$$\int_0^\ell \phi_n^2 \, dx = \ell \quad . \tag{A-4}$$

The nth modal mass of a continuum beam is defined by Eq. (A-5):

$$\int_0^\ell \phi_n^2 \rho(x) \, dx = m_n \quad . \tag{A-5}$$

Since $\rho(x)$ is a constant in this case, Eq. (A-5) is re-expressed as Eq. (A-6):

$$\rho \int_0^\ell \phi_n^2 \, dx = m_n \quad .$$

(A-6)

Substituting Eq. (A-4) into (A-6) yields Eq. (A-3).

The normalized modal shapes of the continuum beam are also used to calculate the mass matrix of the continuum beam, Eq. (A-7):

$$[M] = [\frac{\phi}{\mu}]^{T-1} [\frac{\phi}{\mu}]^{-1} \quad .$$

(A-7)

As before, the normalized mode shapes in $[\phi/\mu]$ correspond to the λ mode shapes of the beam structure being compared to the continuum beam.

ACKNOWLEDGMENTS

41

REFERENCES

1. R. L. Bagley, "Principle of Dynamic Equipollency and the Limitations of the Inverse Eigenvalue Method of Mechanical Admittance Analysis," Technical Note 1974-17, Lincoln Laboratory, M.I.T., 16-25 (4 March 1974).

2. G. J. O'Hara, "Mechanical Impedance and Mobility Concepts," J. Acoust. Soc. of Am., 41, 5,1180-1184 (1967).

3. R. L. Bagley, "Inverse Eigenvalue Method of Mechnical Admittance Analysis," Technical Note 1973-49, Lincoln Laboratory, M.I.T., 11-22 (5 December 1973).

4. F. B. Hildebrand, Methods of Applied Mathematics, 2nd ed., 19 (Prentice-Hall, Englewood Cliffs, N.J., 1965).

5. Wilcoxon Research Bulletins 1-10.

6. Instruction Manual SD-1002B-33 Automatic Mechnical Impedance System, Spectral Dynamics Corp., San Diego, Calif. (August 1968).

7. Bagley, "Inverse Eigenvalue Method...," 23-25.

8. W. C. Hurty and M. F. Rubinstein, Dynamics of Structures, 122-130 (Prentice-Hall, Englewood Cliffs, N.J., 1964).

9. R. L. Bagley, "Antiresonant Frequency and the Measurement of Mechanical Admittance Data," Technical Note 1973-53, Lincoln Laboratory, M.I.T., 15-18 (10 December 1973).

10. Ibid., 26-27.

11. L. L. Bucciarelli, "Some Observations — MM '69 Scan Platform Structural Considerations," Report 605-185, Jet Propulsion Laboratory, California Inst. of Tech., 33 (13 February 1969).

12. Bagley, "Antiresonant Frequency...," 15-25.

13. _____, "Inverse Eigenvalue Method...," 28-32.

14. Ibid., Hildebrand, 19.

15. Bagley, "Inverse Eigenvalue Method...," 28-32.

16. Ibid., Hildebrand, 19.

17. D. Young and R. P. Felgar, Jr., "Tables of Characteristic Functions Representing Normal Modes of Vibrations of a Beam," Univ. of Texas Publ., 49.3, 14-24 (1949).

18. Ibid., 10.

19. Ibid., 11.

20. Ibid., 14-24.

21. Ibid., 9.

REPORT DOCUMENTATION PAGE		READ INSTRUCTIONS BEFORE COMPLETING FORM
1. REPORT NUMBER ESD-TR-75-134	2. GOVT ACCESSION NO.	3. RECIPIENT'S CATALOG NUMBER
4. TITLE *(and Subtitle)* Applications of the Principle of Dynamic Equipollency to Mechanical Admittance Testing		5. TYPE OF REPORT & PERIOD COVERED Technical Note
		6. PERFORMING ORG. REPORT NUMBER Technical Note 1975-20
7. AUTHOR*(s)* Bagley, Ronald L.		8. CONTRACT OR GRANT NUMBER*(s)* F19628-73-C-0002
9. PERFORMING ORGANIZATION NAME AND ADDRESS Lincoln Laboratory, M.I.T. P.O. Box 73 Lexington, MA 02173		10. PROGRAM ELEMENT, PROJECT, TASK AREA & WORK UNIT NUMBERS Project No. 649L
11. CONTROLLING OFFICE NAME AND ADDRESS Air Force Systems Command, USAF Andrews AFB Washington, D.C. 02331		12. REPORT DATE 10 March 1975
		13. NUMBER OF PAGES 56
14. MONITORING AGENCY NAME & ADDRESS *(if different from Controlling Office)* Electronic Systems Division Hanscom AFB Bedford, MA 01731		15. SECURITY CLASS. *(of this report)* Unclassified
		15a. DECLASSIFICATION DOWNGRADING SCHEDULE
16. DISTRIBUTION STATEMENT *(of this Report)* Approved for public release; distribution unlimited.		
17. DISTRIBUTION STATEMENT *(of the abstract entered in Block 20, if different from Report)*		
18. SUPPLEMENTARY NOTES None		
19. KEY WORDS *(Continue on reverse side if necessary and identify by block number)* dynamic equipollency mechanical admittance analysis moment-rotational velocity impedances inverse eigenvalue method		
20. ABSTRACT *(Continue on reverse side if necessary and identify by block number)*		

The principle of dynamic equipollency is defined and applied to two areas of mechanical admittance/impedance testing: generation of experimental moment-rotational velocity admittances and impedances, and many-DOF structures.